Supplement: A new approach to inferring basal drag and ice rheology in ice streams, with applications to West Antarctic ice streams

Meghana RANGANATHAN,[1] Brent MINCHEW,[1] Colin R. MEYER,[2] G. Hilmar GUDMUNDSSON[3]

[1]*Department of Earth, Atmospheric and Planetary Sciences, Massachusetts Institute of Technology, Cambridge, MA, USA*

[2]*Thayer School of Engineering, Dartmouth College, Hanover, NH, USA*

[3]*Geography and Environmental Sciences, Northumbria University, Newcastle upon Tyne, UK*

Correspondence: Meghana Ranganathan <meghanar@mit.edu>

Table S1. Slipperiness parameters from Equation 13, to define the synthetic "true" slipperiness distribution (with x_i and y_i in kilometers, and $d_x = d_y = 250$).

i	x_i	y_i	a_i
1	0	0	40
2	70	7	100
3	-70	7	5
4	70	-7	10
5	-40	-7	5
6	20	8	100
7	-70	3	20
8	60	-7	10
9	-50	3	70
10	-30	3	20
11	20	-7	10
12	-10	-9	70

Table S2. Regularization coefficients at the start of the inversion for a high-frequency slipperiness field. The inversion was run multiple times, with decreasing regularization coefficients and setting the result of the previous inversion as the prior of the next iteration. The initial regularization coefficients are listed below as "start" and the final values are listed as "finish". We define $[c]$ as the units of slipperiness ($[c] = $ m a^{-1} kPa^{-3}), $[A]$ as the units of the flow-rate parameter ($[A] = $ a^{-1} kPa^{-3}), $[\nabla c]$ as the units of the gradient of slipperiness, and $[\nabla A]$ as the units of the gradient of the flow-rate parameter. Curly brackets denote the units for the full coefficient (g_{s_i} and g_{a_i} for $i = [A, c]$). For the coefficients with strain rates, the floating mask is not shown since the model domain is fully grounded. Thus, the formulation shown in Equations 13 and 14 simplifies to what is shown here.

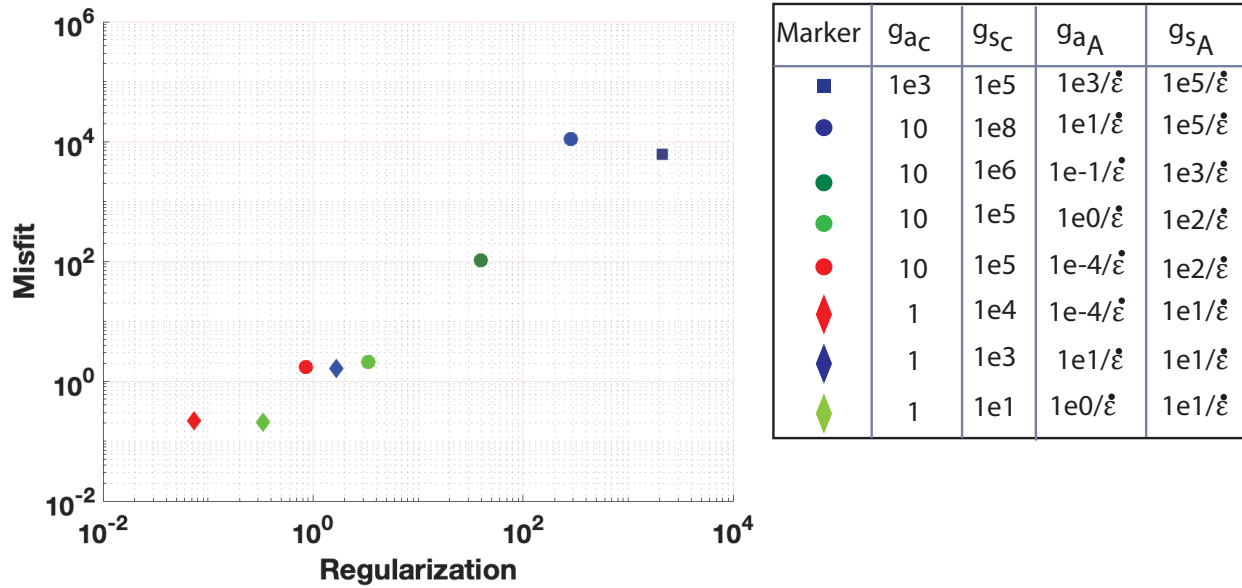|	**No Strain Rates**		**Strain Rates**	
	c	**A**	**c**	**A**
$\mathbf{g_s}$(start)	1e5 $\{[\nabla c]^{-2}\}$	1e4 $\{[\nabla A]^{-2}\}$	1e5 $\{[\nabla c]^{-2}\}$	100 $\dot{\epsilon}_e^{-1}$ $\{[\nabla A]^{-2}\}$
$\mathbf{g_a}$(start)	10 $\{[c]^{-2}\}$	1 $\{[A]^{-2}\}$	10 $\{[c]^{-2}\}$	$(100\,\dot{\epsilon}_e)^{-1}$ $\{[A]^{-2}\}$
$\mathbf{g_s}$(finish)	1e3 $\{[\nabla c]^{-2}\}$	1e2 $\{[\nabla A]^{-2}\}$	1e3 $\{[\nabla c]^{-2}\}$	$\dot{\epsilon}_e^{-1}$ $\{[\nabla A]^{-2}\}$
$\mathbf{g_a}$(finish)	0.5 $\{[c]^{-2}\}$	1 $\{[A]^{-2}\}$	0.25 $\{[c]^{-2}\}$	$(100\,\dot{\epsilon}_e)^{-1}$ $\{[A]^{-2}\}$

Fig. S1. Varying regularization coefficients and their outputs in terms of resulting regularization and resulting misfit on a log-log plot. We test a variety of regularization coefficients to show that many result in very poor convergence (high regularization and high misfit) and others produce much better convergence. From preliminary tests that show the importance of g_{a_c} and g_{a_A} in determining convergence, we show varying g_{a_c} by varying Markers and we show varying g_{a_A} by varying colors. Smaller values of g_{a_c} generally produce better convergence ($g_{a_c} = 1$ producing the best results in this preliminary examination). Further, lower values of g_{a_A} produce better results than higher values, with some deviations from this. The balances used in the synthetic experiments presented in this paper produce relatively low regularization and misfit. We began the inversions with higher regularization (approximately near the dark green circle). Once that problem has reached a minimum, we restart the inversion with a lower regularization (approximately the red circle) and with the estimates of the initial inverse problem as the priors. We continue reducing the regularization and running new inversions, using the previous estimate as the starting point, until we have produced reasonable estimates (the misfit has fallen below data errors) (approximately the red diamond). This ultimately results in good convergence. The convergence of the inversion is clearly quite sensitive to choices of the regularization coefficients and a much wider study would be useful in elucidating the proper balance of regularization for glaciological inversions.
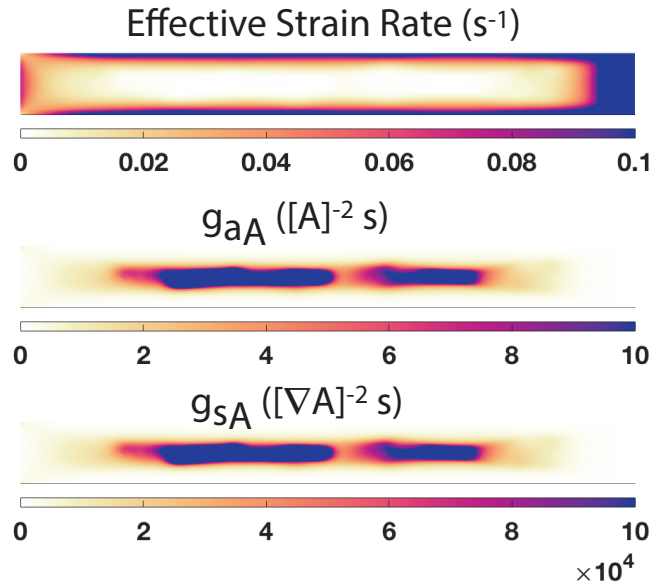
Effective Strain Rate (s⁻¹)

g_{aA} ([A]⁻² s)

g_{sA} ([∇A]⁻² s)

×10⁴

Fig. S2. Regularization fields for the synthetic test with strain rates for the test presented in Figure 1 of the main text: (a) The effective strain rates for the synthetic test with a high-frequency slipperiness field, in which the strain rates are high in the margins and near the grounding line and low in the centerline, (b) the regularization coefficient applied to the departure of the flow rate parameter from the prior, in which we penalize changes in the centerline, (c) the regularization coefficient applied to the departure of the gradient of the flow rate parameter from the prior, in which we similarly penalize changes in the centerline. The values are approximately a similar magnitude as the regularization for the synthetic test without strain rates.
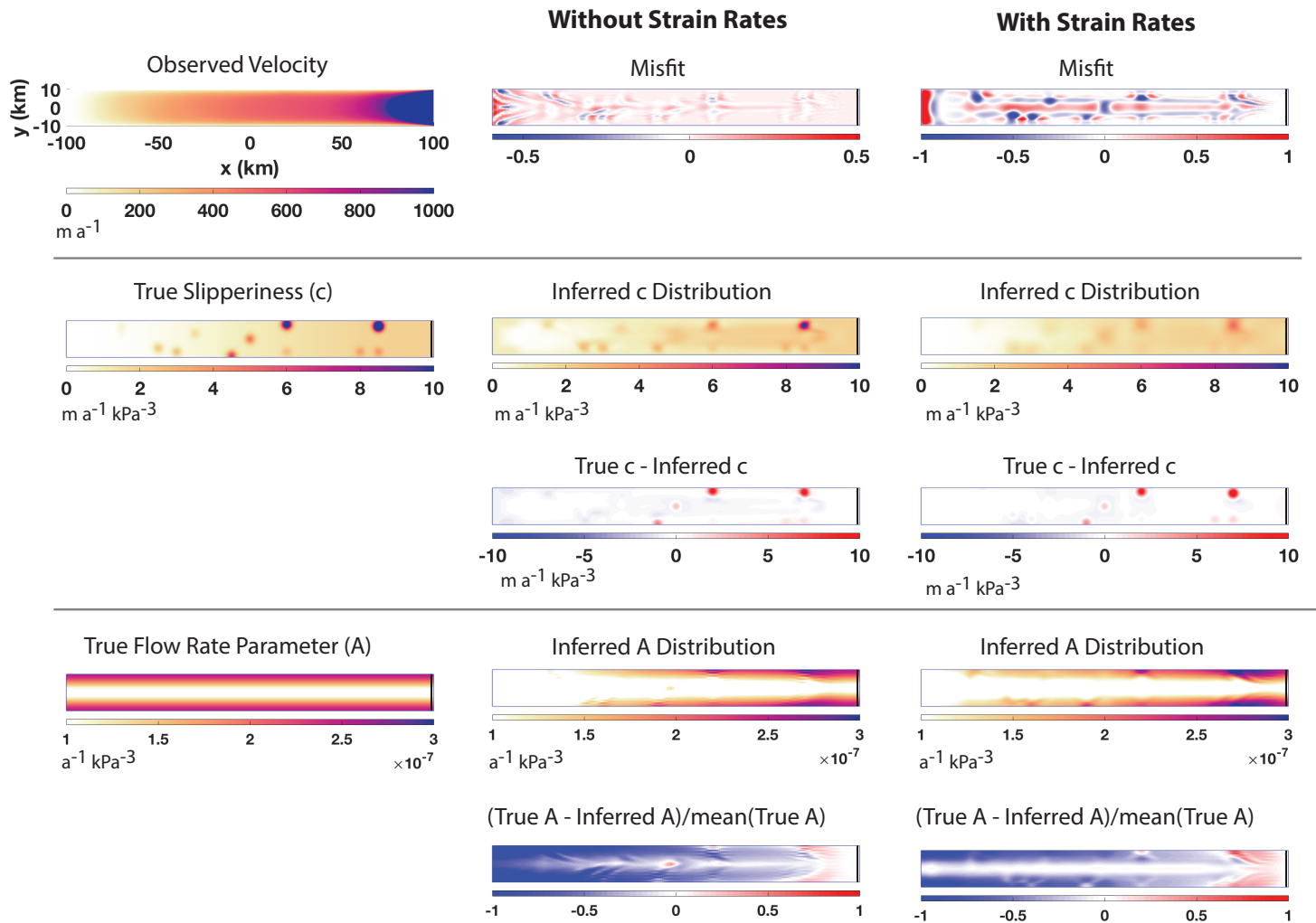
Fig. S3. Results from two synthetic tests with a mixed-frequency slipperiness field. The left column shows observed velocity (synthetic velocity set as measured velocity in the inversion), the prescribed "true" slipperiness distribution (with slippery spots represented as Gaussian spikes and a long-wavelength background field in which slipperiness increases closer to the grounding line), and the prescribed "true" flow rate parameter distribution (with high values in the lateral shear margins, where ice is softer due to viscous deformation). The middle column presents results with spatially constant regularization values. The inversion does not properly capture the long-wavelength variation in the slipperiness field and underestimates the flow rate parameter upstream of the grounding line. There is mixing in the centerline of the flow rate parameter distribution. Mixing is less significant than it was in the high-frequency synthetic test. The right column presents results from an inversion where the flow rate parameter regularization values are scaled by strain rates. This eliminates the mixing in the flow rate parameter distribution and improves the estimation of the magnitude of slippery spots in the slipperiness distribution. This improves the estimation of the long-wavelength slipperiness field, though it decreases the the magnitude of the Gaussian spikes. Finally, it improves estimation of the flow rate parameter upstream of the grounding line.
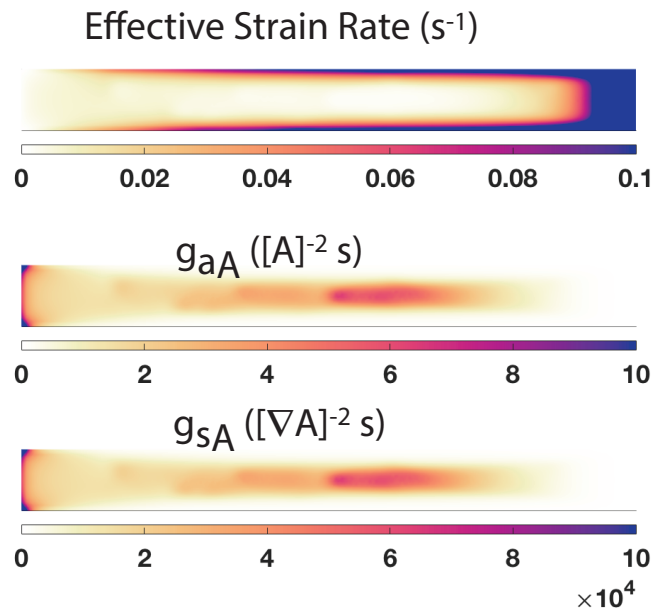
Fig. S4. Regularization fields for the synthetic test with strain rates for the mixed-frequency slipperiness field (e.g. Figure S3 of the Supplement): (a) The effective strain rates for the synthetic test with a mixed-frequency slipperiness field, in which the strain rates are high in the margins and near the grounding line and low in the centerline, (b) the regularization coefficient applied to the departure of the flow rate parameter from the prior, in which we penalize changes in the centerline, (c) the regularization coefficient applied to the departure of the gradient of the flow rate parameter from the prior, in which we similarly penalize changes in the centerline. The values are approximately a similar magnitude as the regularization for the synthetic test without strain rates.
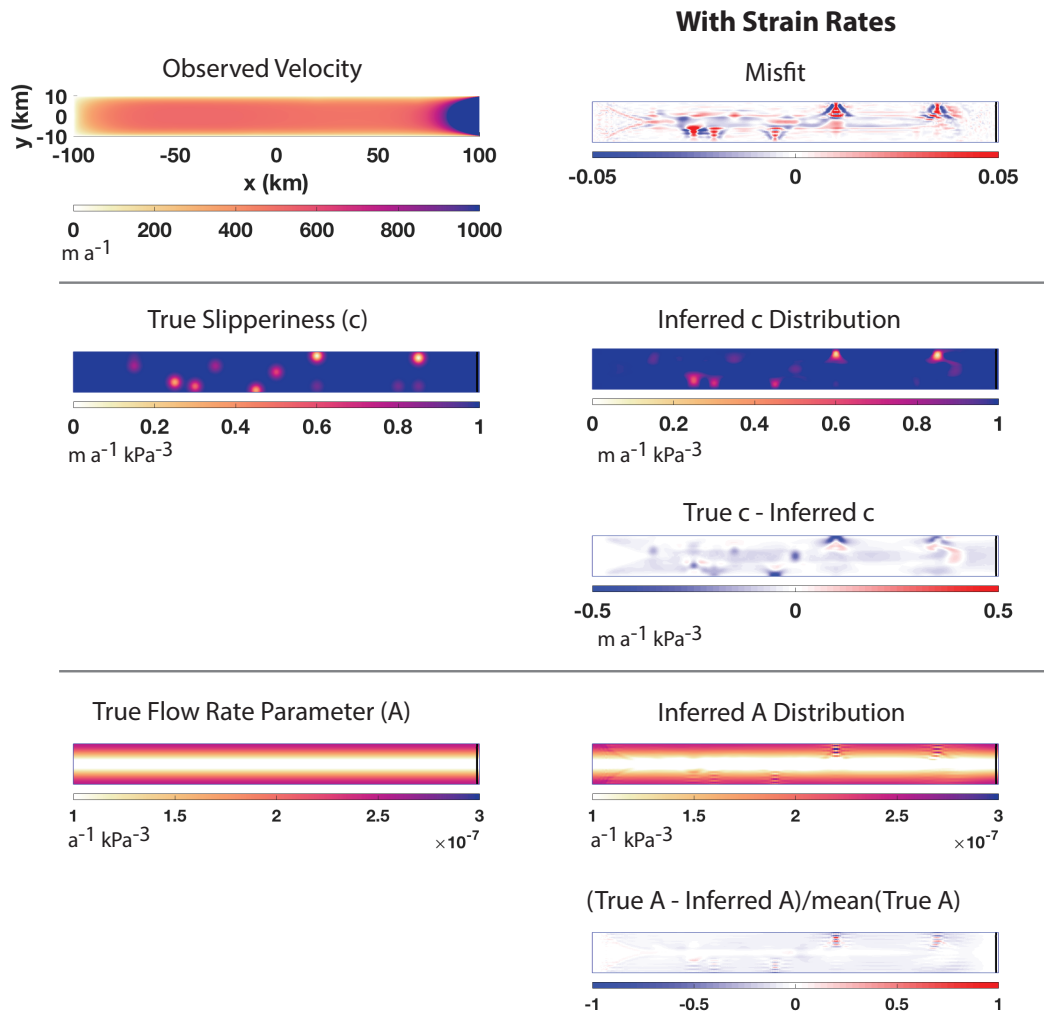
Fig. S5. Results from a synthetic test with sticky spots. The left column shows observed velocity (synthetic velocity set as measured velocity in the inversion), the prescribed "true" slipperiness distribution (with sticky spots represented as Gaussian spikes), and the prescribed "true" flow rate parameter distribution (with high values in the lateral shear margins, where ice is softer due to viscous deformation). The second column presents results from an inversion where the flow rate parameter regularization values are scaled by strain rates. The sticky spots are captured by the inversion, maintaining the constant background field. There is one misplaced Gaussian bump near the grounding line. The flow rate parameter shows little mixing between the two estimates and the inversion reproduces the spatial distribution.
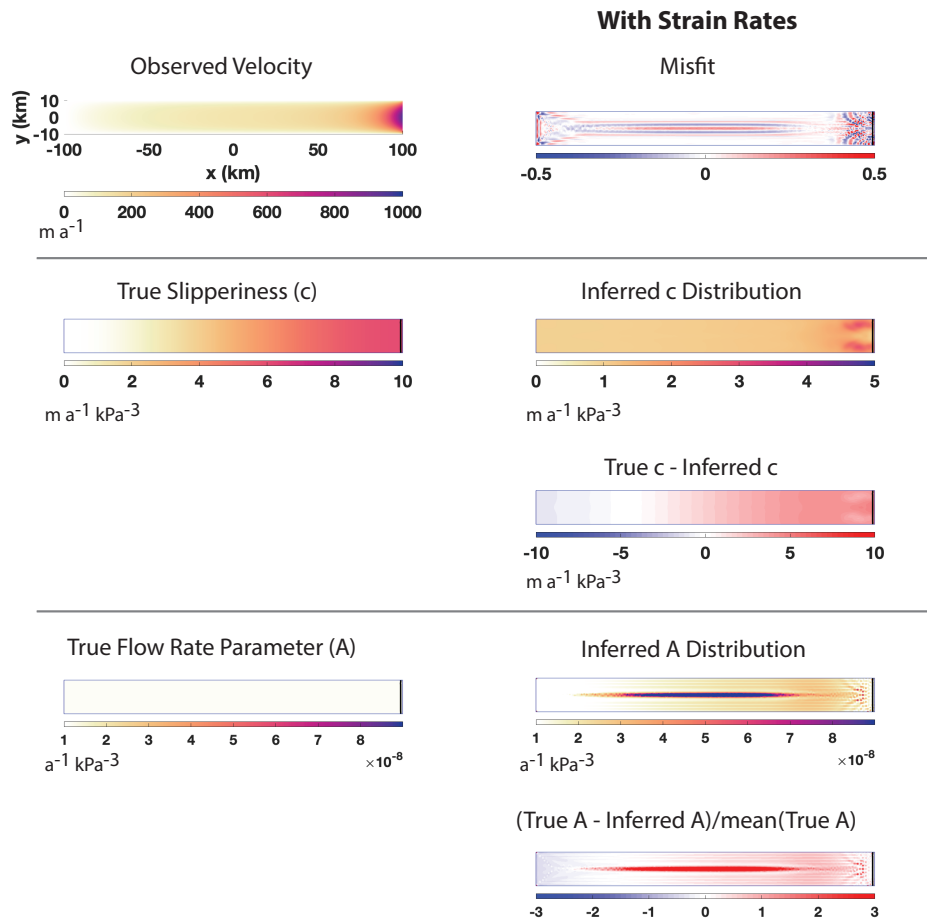
With Strain Rates

Observed Velocity

Misfit

True Slipperiness (c)

Inferred c Distribution

True c - Inferred c

True Flow Rate Parameter (A)

Inferred A Distribution

(True A - Inferred A)/mean(True A)

Fig. S6. Results from a synthetic test with a constant true flow-rate parameter field (of value about 1×10^{-8}). The true slipperiness has a low-frequency variation in which basal slipperiness increases steadily towards the grounding line. Variations of the basal slipperiness coefficient and the flow rate parameter are in the same direction. A constant flow-rate parameter as shown here is unlikely in Antarctic ice streams, due to the softening mechanisms acting in the margins, and given the formulation of the approach defined in this paper, we do not expect the approach to minimize mixing in this case, particularly in the centerline where strain rates are low. The prior of the flow-rate parameter is a constant of value 8×10^{-8} and the prior of the basal slipperiness coefficient is also a constant of value 1. While the inferred slipperiness distribution does increase, it fails to capture the long-wavelength variation. Furthermore, while the inference of the flow-rate parameter in the margins is more accurate, the flow-rate parameter estimate does not succeed in capturing the true field in the centerline as expected, since there is no information about the flow-rate parameter in areas with slow deformation rates. Finally, there is a long-wavelength variation in the flow-rate parameter field that is likely due to mixing between the two parameters.
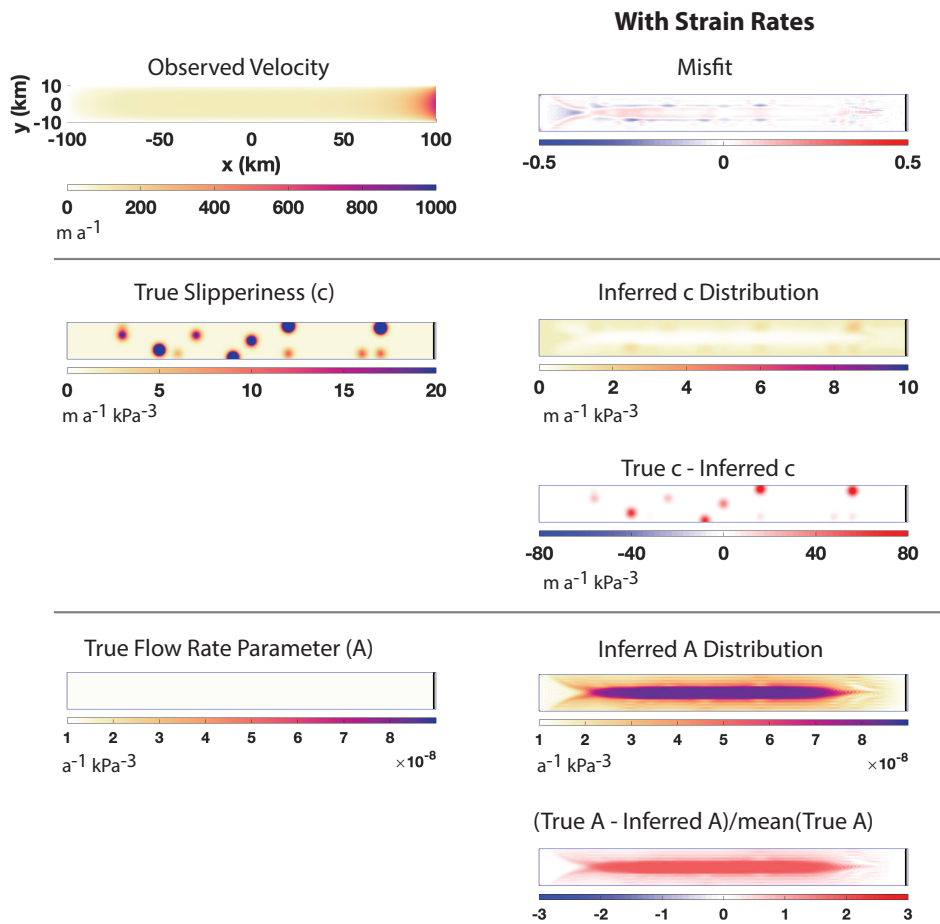
Fig. S7. Results from a synthetic test with a constant true flow-rate parameter field (of value about 1×10^{-8}). The true slipperiness has high-frequency variation, in which there are localized spots of high slipperiness along the length of the ice stream. Variations of the basal slipperiness coefficient and the flow rate parameter are in the same direction. Again, we have reason to believe that this case is unlikely in Antarctic ice streams. The prior of the flow-rate parameter is a constant of value 8×10^{-8} and the prior of the basal slipperiness coefficient is also a constant of value 1. While the inferred slipperiness distribution does capture the slippery spots, it fails to capture the magnitude of these spots. Furthermore, the estimated field has a decreased slipperiness in the centerline not seen in the true distribution, likely from mixing between the two parameters. The inferred flow-rate parameter distribution successfully captures the true distribution in the margins but has erroneously high values in the centerline, suggesting that this approach again does not apply for a situation with a flow-rate parameter that is not higher in the margins than in the centerline.

Table S3. Regularization coefficients at the start of the inversion for a mixed-frequency slipperiness field. The inversion was run multiple times, with decreasing regularization coefficients and setting the result of the previous inversion as the prior of the next iteration. The initial regularization coefficients are listed below as "start" and the final values are listed as "finish". We define $[c]$ as the units of slipperiness ($[c] = $ m a^{-1} kPa^{-3}), $[A]$ as the units of the flow-rate parameter ($[A] = $ a^{-1} kPa^{-3}), $[\nabla c]$ as the units of the gradient of slipperiness, and $[\nabla A]$ as the units of the gradient of the flow-rate parameter. Curly brackets denote the units for the full coefficient (g_{s_i} and g_{a_i} for $i = [A, c]$). . For the coefficients with strain rates, the floating mask is not shown since the model domain is fully grounded. Thus, the formulation shown in Equations 13 and 14 simplifies to what is shown here.

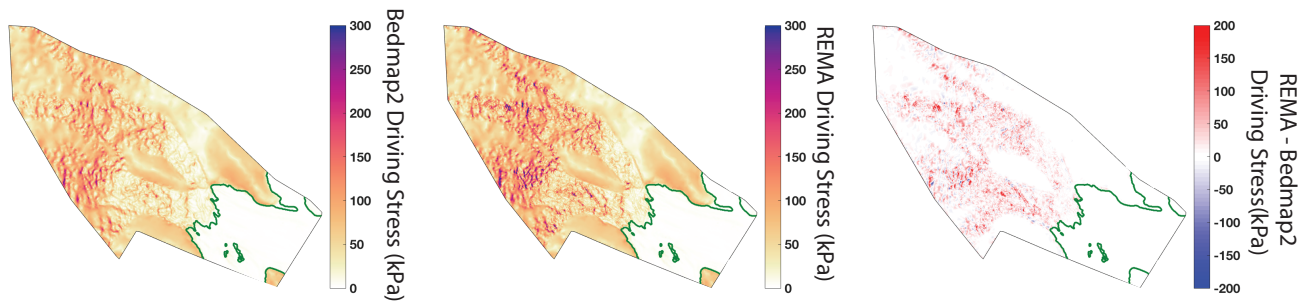|	*No Strain Rates*		*Strain Rates*	
	c	**A**	**c**	**A**
$\mathbf{g_s}$(start)	1e5 $\{[\nabla c]^{-2}\}$	1e4 $\{[\nabla A]^{-2}\}$	1e5 $\{[\nabla c]^{-2}\}$	1000 $\dot{\epsilon}_e^{-1}$ $\{[\nabla A]^{-2}\}$
$\mathbf{g_a}$(start)	10 $\{[c]^{-2}\}$	1 $\{[A]^{-2}\}$	10 $\{[c]^{-2}\}$	$(10\ \dot{\epsilon}_e)^{-1}$ $\{[A]^{-2}\}$
$\mathbf{g_s}$(finish)	1e3 $\{[\nabla c]^{-2}\}$	1e2 $\{[\nabla A]^{-2}\}$	1e4 $\{[\nabla c]^{-2}\}$	100 $\dot{\epsilon}_e^{-1}$ $\{[\nabla A]^{-2}\}$
$\mathbf{g_a}$(finish)	1 $\{[c]^{-2}\}$	1 $\{[A]^{-2}\}$	1 $\{[c]^{-2}\}$	$(500\ \dot{\epsilon}_e)^{-1}$ $\{[A]^{-2}\}$

Fig. S8. The driving stress of Bindschadler and MacAyeal ice streams computed by (a) Bedmap2 surface elevation, (b) REMA surface elevation. (b) The driving stress is higher over the length of the ice streams with the higher-resolution REMA data than with Bedmap2 data. Results from the inversions on Bindschadler and MacAyeal presented here are updated from similar inversions due to more accurate, higher-resolution data.
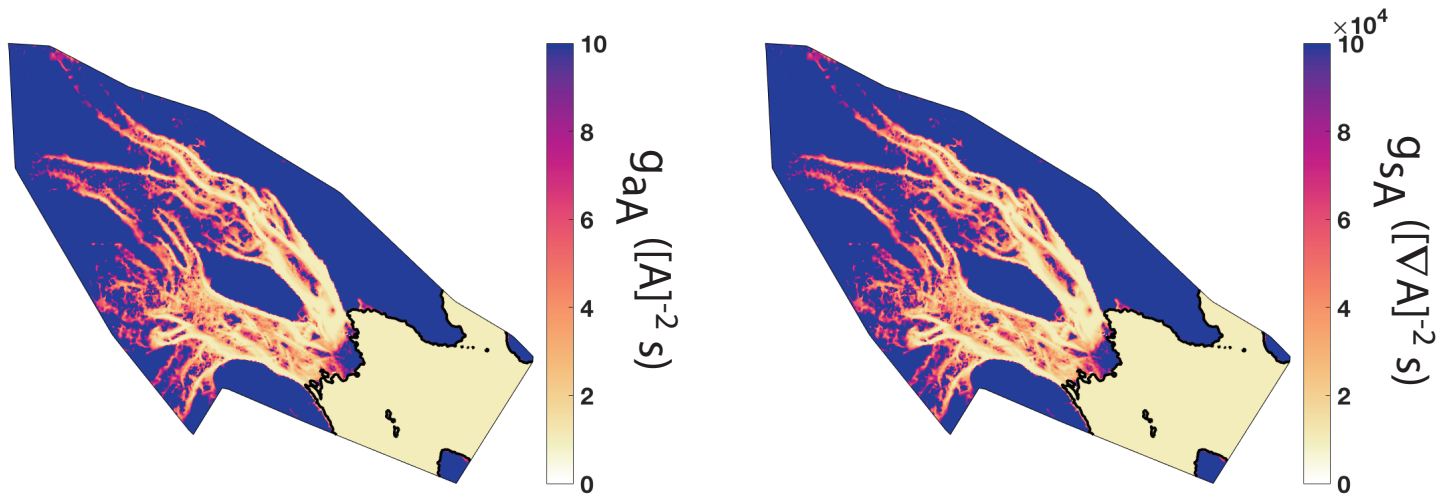
Fig. S9. Regularization fields for the inversion on Bindschadler and MacAyeal ice streams: (a) the regularization coefficient applied to the departure of the flow rate parameter from the prior, in which the lowest values are applied to the margins and the highest values are outside of the ice streams, (b) the regularization coefficient applied to the departure of the gradient of the flow rate parameter from the prior, in which we similarly see lowest values in the margins and highest values outside of the ice streams. Changes in the regularization coefficients with strain rates are not applied to the ice shelf. Regularization coefficients are similar to those found in the high frequency synthetic test.
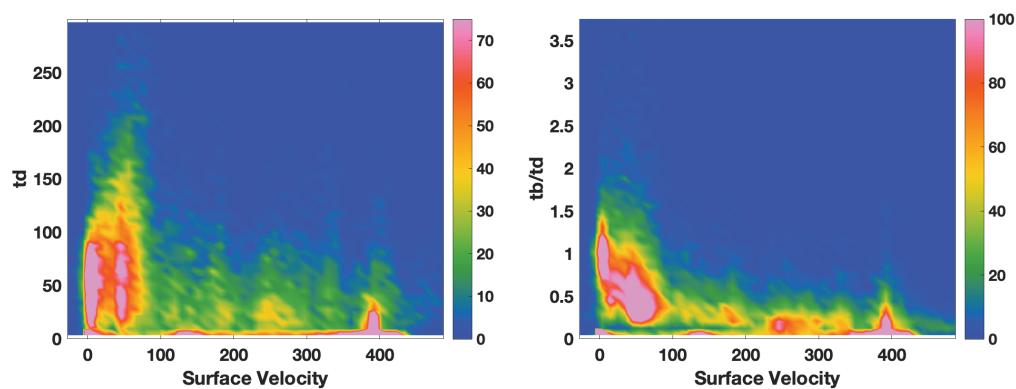
Fig. S10. Density plots of surface velocity and: (a) driving stress, in which the profile suggests faster velocities for lower driving stresses. This provides evidence for the ice streams slipping relative to their bed, since the velocities depend not only on driving stress but also on excess stress, (b) the ratio of basal drag to driving stress, providing further evidence of slipping relative to the bed, since basal drag must be a primary resistance to driving stress.
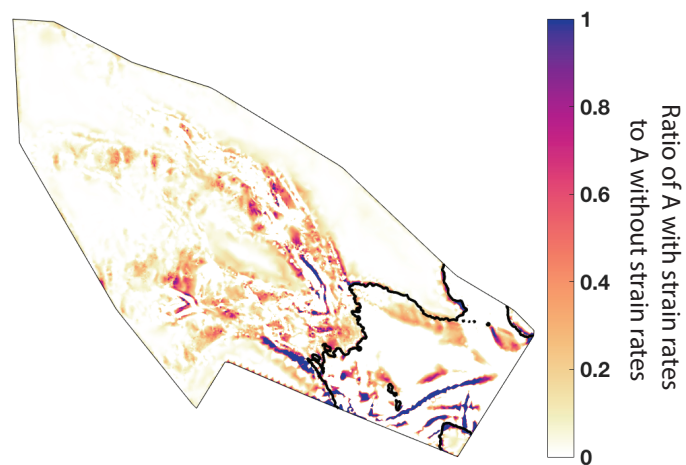
Fig. S11. The ratio of inferred flow rate parameter found with strain rates to that found without strain rates, in which the ratio remains of order 1 or less. With strain rates, the inference is lower on average than without. The most significant differences occur in the northern shear margin of MacAyeal and over the ice shelf, where pinning points may be causing errors in the inference.